Asymmetric Contact-Induced Self-Driven Perovskite-Microwire-Array Photodetectors

Chun-Yan Wu, Wei Peng, Ting Fang, Bin Wang, Chao Xie,* Li Wang, Wen-Hua Yang, and Lin-Bao Luo*

Combining both 1D geometry and the features of hybrid perovskite materials, perovskite micro/nanowires have recently attracted particular attention for a variety of optoelectronic device applications. Herein, by taking advantage of the strong built-in potential induced by asymmetric contact with varied work functions, highly sensitive visible photodetectors based on a $CH_3NH_3PbI_3$ microwire array that display pronounced photovoltaic activities are reported. These photodetectors afford the capability to work without an external power supply. A representative detector with Au/Ag electrodes achieves a reasonable responsivity of 161.1 mA W^{-1} with a fast response speed of 13.8/16.1 µs under 520 nm illumination at zero bias. In addition, such a device is also characterized by an ultralow dark current of tens of femtoamps, enabling a high specific detectivity of 1.3×10^{12} Jones. Furthermore, a flexible photodetector is successfully prepared, which shows comparable photoresponse performance and outstanding flexibility and bending durability. Given the good device performance and simple device geometry, the present self-driven photodetectors hold great promise for future highly sensitive and low-energy-consumption photodetection systems.

1. Introduction

In recent years, organic–inorganic hybrid perovskites have been widely exploited for applications in many optoelectronic devices such as solar cells, light-emitting diodes, photodetectors, and semiconductor lasers.[1–8] As one group of the most promising optoelectronic semiconductors, perovskite possess a variety of appealing physical and optoelectronic properties, e.g., strong optical absorption coefficient, high carrier mobility, long carrier diffusion length, solution-based processibility and so on.[9–11] To date, different types of photodetectors, which can convert optical signals into electrical signals and are key components in optoelectronic systems, have been realized using perovskite materials in the form of thin films, bulk single-crystals, and microwires/ nanowires (MWs/NWs).[12–16] These detectors have achieved excellent photoresponse performance that can compete with

traditional semiconductor devices. However, although thin films of perovskites can be prepared easily in large-scale through some facile solution-based processes, the presence of some intrinsic problems inevitably restricts further improvement of device performance. For example, perovskite thin films usually have polycrystalline structures with numerous defects and grain boundaries, which reduce carrier mobility and shorten carrier lifetime by acting as trapping and scattering centers for charge carriers.[17,18] Additionally, a large amount of grain boundaries that are susceptible to moisture can also reduce device stability in ambient condition.[19] In comparison, single-crystalline perovskites possessing much lower defect concentration and fewer grain boundaries can have a far higher carrier mobility and longer carrier lifetime, and are also more stable when placed in air.[20–22] Nevertheless, growth of perovskite bulk single-crystals often requires usage of enormous amounts of perovskite precursor materials, which makes optoelectronic devices uneconomical. In addition, device miniaturization has also been ruled out because of the extremely large size of the bulk single-crystals. To this end, 1D perovskite MWs/NWs with well-defined single-crystalline structures can be promising candidates for assembling high-performance and cost-effective perovskite photodetectors with reasonable air stability. In addition to the above-mentioned merits, 1D perovskite MWs/NWs can also provide other advantages such as uniform pathways for efficient charge carrier transport, large surface-to-volume ratio for superior antireflection, and strong light trapping, as well as excellent mechanical flexibility bringing opportunity for assembling photodetectors on polymer substrates toward flexible, deformable, and wearable optoelectronics.[23,24]

So far, several approaches have been developed to prepare high-quality perovskite MWs/NWs for high-performance optoelectronic devices.[25–29] For example, perovskite NWs array with single-crystalline structures can be easily grown in large-scale via a one-step solvent evaporation induced self-assembly method.[26] By using this technique, a photodetector based on array of $CH_3NH_3PbI_3$ NWs have been constructed, which showed responsivity and specific detectivity of 1.32 A W^{-1} and 2.5×10^{12} Jones, respectively, along with a response speed of 0.3 ms. Jie and co-workers also reported large-scale preparation of aligned single-crystalline perovskite MWs array through a

Prof. C.-Y. Wu, W. Peng, T. Fang, B. Wang, Dr. C. Xie, Dr. L. Wang, Dr. W.-H. Yang, Prof. L.-B. Luo
School of Electronic Science and Applied Physics
Hefei University of Technology
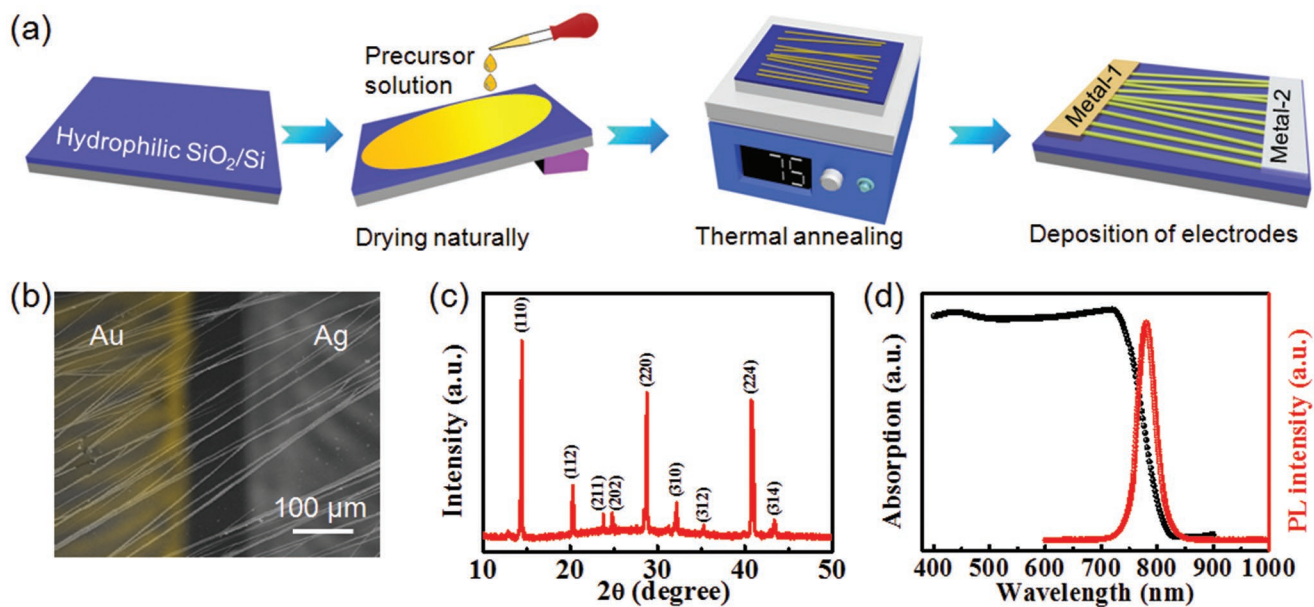Hefei, Anhui 230009, China
E-mail: chao.xie@hfut.edu.cn; luolb@hfut.edu.cn

Figure 1. a) Schematic illustration of stepwise process for fabricating $CH_3NH_3PbI_3$ MWs array based photodetector with asymmetric contact electrodes. b) FESEM image of a typical photodetector with Au/Ag electrode pair. c) XRD pattern and d) absorption and PL spectra of as-fabricated $CH_3NH_3PbI_3$ MWs array.

simple blade-coating method, and a $CH_3NH_3PbI_3$ MWs array-based photodetector attained responsivity and specific detectivity of 13.57 A W^{-1} and 5.25×10^{12} Jones, respectively.[27] The detector exhibited an acceptable response speed with rise/decay times of 80/240 µs. From the view of many crucial applications (e.g., rapid data transmission, high-speed optical communication, military warning, fast imaging, etc.), high-frequency light detection is essentially required.[30,31] Various recent studies have also proven that due to the inherent built-in potential that accelerates photocarrier separation and transport processes, photovoltaic (PV)-type perovskite detectors usually possess much faster response speed together with a lower noise level, in comparison with other types of perovskite photodetectors.[32–35] However, to the best of our knowledge, PV-type photodetectors employing perovskite MWs/NWs as the photoactive materials have been far scarcely explored to date.

In this work, we present the design of high-performance perovskite photodetectors, which are composed essentially of $CH_3NH_3PbI_3$ MWs array with asymmetric contact. Such asymmetric contact electrodes with different work functions introduce a strong built-in potential across the MWs, which affords our devices with apparent PV activities and thus allows them to function as self-driven photodetectors. By optimizing the contact electrodes, good photoresponse performance in terms of a decent responsivity of 161.1 mA W^{-1} and rapid response speed of 13.8/16.1 µs has been attained for a detector with Au/Ag asymmetric contacts upon 520 nm irradiation at zero bias. Additionally, the device exhibits an ultralow dark current in the order of tens of fA, which renders a high specific detectivity of 1.3×10^{12} Jones. We also assemble flexible photodetectors on polymer substrates, which show comparable photoresponse properties with those on rigid substrates. Further bending tests reveal excellent flexibility and bending durability of the flexible detectors.

2. Results and Discussion

The self-driven photodetectors based on $CH_3NH_3PbI_3$ MWs array with asymmetric contact were fabricated following the schematic illustration shown in **Figure 1**a. In brief, $CH_3NH_3PbI_3$ MWs array with preferential growth direction were first prepared on a hydrophilic-treated SiO$_2$/Si substrate via the solvent evaporation induced self-assembly method reported previously.[26] Then, after thermal annealing to improve the crystalline quality of the MWs, electrodes with different work functions were deposited sequentially on opposite sides of the MWs through electron-beam evaporation by using a lab-built shadow mask. Figure 1b shows the field emission scanning electron microscopy (FESEM) image of an as-constructed device with Au/Ag asymmetric contacts. Apparently, aligned MWs array crossed over asymmetric contact electrodes, forming a typical metal-semiconductor-metal (MSM) photodetector. According to the statistical MW diameter distribution (Figure S1, Supporting Information), the typical diameter of the MWs is mostly in the range of 1–3 µm. In addition, it was observed that the as-grown MWs had relatively smooth and clean surface, implying a good crystalline quality of the MWs. The as-obtained MWs were further characterized by X-ray diffraction (XRD). As depicted in Figure 1c, the diffraction peaks at 14.22°, 28.44°, 31.78°, 40.48°, and 43.04° can be indexed to (110), (220), (310), (224), and (314) planes, respectively, which indicates a well crystallized tetragonal structure with $a = 8.855$ Å and $c = 12.659$ Å.[36] Figure 1d displays the UV–vis absorption and photoluminescence (PL) spectra of the $CH_3NH_3PbI_3$ MWs. The MWs exhibited broadband absorption in the visible region with a distinct absorption edge at ≈800 nm. The PL peak was located at ≈780 nm with the full width at half-maximum (FWHM) of less than 40 nm. The above results are consistent with those of $CH_3NH_3PbI_3$ single-crystals

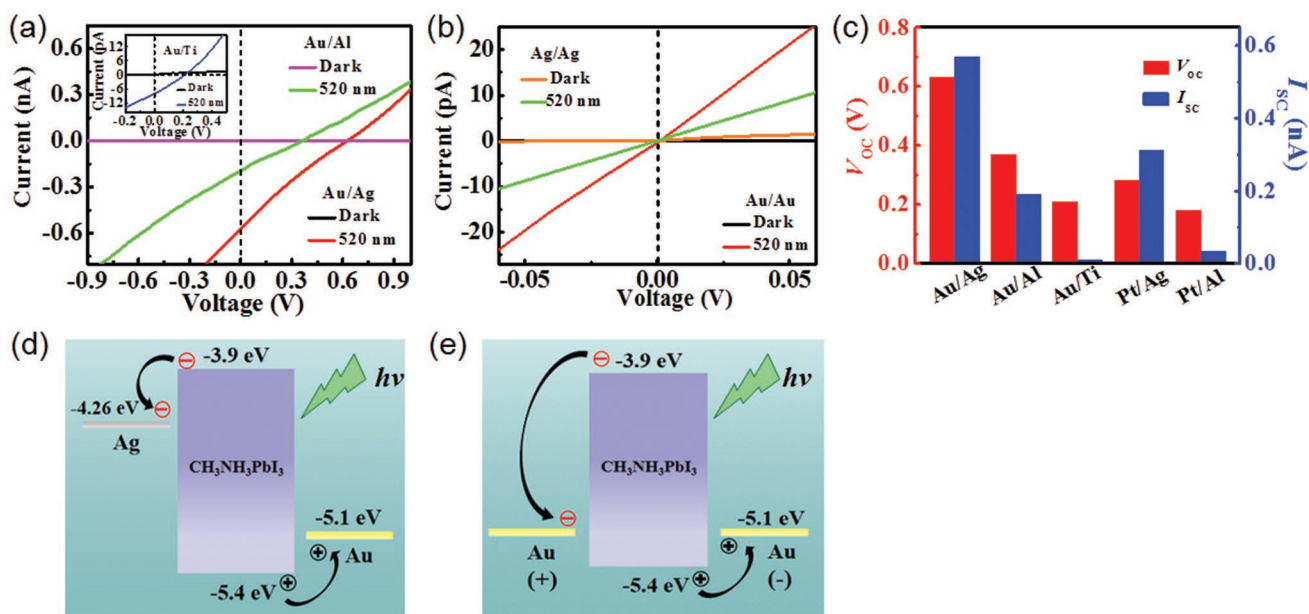**Figure 2.** I–V curves of the $CH_3NH_3PbI_3$ MWs array based photodetectors with a) asymmetric contact electrodes (Au/Ag, Au/Al) and b) symmetric contact electrodes (Au/Au, Ag/Ag) in dark and upon 520 nm light illumination. Inset in (a) shows the I–V curves of the device with Au/Ti contact electrodes in dark and upon 520 nm light illumination. c) Histogram of V_{OC} and I_{SC} for devices with different asymmetric electrodes pairs. Energy band diagrams of the device with d) Au/Ag asymmetric electrodes and e) Au/Au symmetric electrodes upon light illumination.

in literatures, suggesting that $CH_3NH_3PbI_3$ MWs with good crystallinity have been successfully synthesized.[20,21]

To implement the self-driven photodetection function of the $CH_3NH_3PbI_3$ MWs, various photodetectors composed of metal electrodes with both a high work function (Au or Pt) and a low work function (Ag, Al, or Ti) on opposite sides of the MWs were constructed. The photoresponse properties of those devices having nearly identical density of MWs across the device channel were studied and compared. **Figure 2**a and Figure S2 (Supporting Information) plot the current–voltage (I–V) characteristics of some representative devices with asymmetric electrode pairs of Au/Ag, Au/Al, Au/Ti, Pt/Ag, and Pt/Al, measured in dark and under the same illumination condition (520 nm, 27.12 mW cm^{-2}). It was observed that these devices showed extremely low channel current in dark (Figure S2a, Supporting Information). The nonlinear I–V behaviors also indicate existence of Schottky barriers at MW-metal contacts. Interestingly, when shined by light irradiation, the I–V curves of all devices deviated somewhat from the coordinate origin, giving rise to obvious PV effects. This phenomenon was completely different from control devices with symmetric electrode pair of Au/Au or Ag/Ag, whose I–V curves under irradiation went through the coordinate origin, implying no PV activity (Figure 2b). In addition, we also found that the observed PV activities varied significantly between devices with different asymmetric electrode pairs, and the strongest PV effect was found for the detector with Au/Ag electrode pair with a maximum open-circuit voltage (V_{OC}) of 0.62 V and short-circuit current (I_{SC}) of 0.57 nA, respectively (Figure 2c).

The above observations can be illustrated by analyzing the energy band diagrams and charge transfer processes of the devices. Due to the difference in work functions between $CH_3NH_3PbI_3$ MW and metal electrode, charge transfer would take place when two materials contact with each other, leading to a Schottky barrier at MW-metal contact.[37] As we discussed previously, the present devices have a typical MSM device geometry. Therefore, the resultant built-in potential in the device channel is determined by the Schottky barrier height difference between two opposite MW-metal contacts.[38] For devices with symmetric contact electrodes (Au/Au or Ag/Ag), the Schottky barrier profiles are mirror symmetric at opposite MW-metal contacts. In this case, the photocarriers (induced by light absorption with a photon energy higher than perovskite bandgap) have no preferred drift direction in the channel, or in other words, the photocurrent is opposite and antisymmetric near both MW-metal contacts, leading to zero net photocurrent.[39,40] Thus, an applied bias voltage is required to separate photoexcited electrons and holes, and give rise to photocurrent (Figure 2b,e). On the other hand, when asymmetric electrodes are used, mirror symmetry in the Schottky barrier profile will be broken because of different barrier heights at opposite MW-metal contacts, which consequently gives a built-in potential in the device channel responsible for generation of photocurrent at zero bias.[39,40] Specifically, in the device with Au/Ag electrode pair, when the MW communicates with the electrodes, electrons will flow from MW (Ag) to Au (MW) because of lower (higher) work function of Au (Ag) relative to the Fermi level of single-crystalline $CH_3NH_3PbI_3$ MW considering their near intrinsic semiconductor nature.[41] As a result, a built-in potential with the direction from MW (Ag) to Au (MW) is formed near the MW-Au (MW-Ag) contact. Consequently, the two potentials with the same direction give rise to a strong built-in potential across the whole MW channel. Upon light irradiation, photocarriers within the MWs can easily diffuse to the Schottky barrier regions due to their extremely long diffusion length,[20,21] and then be separated by the built-in potential. Subsequently,

**ADVANCED
SCIENCE NEWS**
www.advancedsciencenews.com

**ADVANCED
ELECTRONIC
MATERIALS**
www.advelectronicmat.de

electrons and holes are quickly extracted by Ag and Au electrodes, respectively, leading to generation of sizeable photocurrent at zero bias (Figure 2d). On the other hand, when Al or Ti electrodes are used instead of the Ag electrode, the built-in potential at MW-Al or MW-Ti contact will be reduced due to the slightly larger work function of Al and Ti (Figure S3a,b, Supporting Information). Meanwhile, the surface of evaporated Al and Ti electrodes are more prone to be oxidized, which probably results in formation of interfacial layer at MW-metal interface and also reduces the conductivity of the electrodes. The above issues are likely to be responsible for the reduced PV effects in devices with Au/Al and Au/Ti electrode pairs. In addition, in the case of devices with Pt electrode, because of the higher work function of Pt relative to the conduction band maximum of $CH_3NH_3PbI_3$, a barrier will exist at the MW-Pt contact for extraction of holes (Figure S3c,d, Supporting Information), leading to reduced PV effects in comparison with the detectors with Au electrode.

The pronounced PV effects enable our devices to work as self-driven photodetectors operating at zero bias.[42,43] We then systematically characterized the photoresponse properties of the detector with Au/Ag electrode pair considering its strongest PV effect. **Figure 3**a plots the $I–V$ characteristics in dark and under 520 nm irradiation (27.12 mW cm^{-2}). Obviously, the device exhibited a high sensitivity to light illumination in the measured bias voltage from −3 to 3 V. The time-dependent photoresponse under periodically switched light illumination was further studied at zero bias. As displayed in Figure 3b, the device can be readily switched between on- and off-states, with a good reproducibility. The dark current was as low as ≈20 fA, while the current upon irradiation reached as high as ≈0.66 nA,

which gave rise to a high I_{light}/I_{dark} ratio of ≈3.3 × 10^4. Such an ultralow dark implies that the present device held great possibility for weak light signal detection.[44] In fact, the photoresponse properties can be well maintained even after hundreds of cycles of operation, suggesting good durability of the photodetector (Figure S4a, Supporting Information). In addition, we found that the photoresponse depended strongly on the applied working bias. As shown in Figure S4b (Supporting Information), the photocurrent increased monotonously with increasing reverse operational voltage (a positive voltage applied to Au electrode is defined as forward operational voltage), which can be ascribed to improved separation of electrons and holes, as well as suppressed recombination activities of photocarriers induced by an external potential in the same direction with the built-in one.

We further explored the light intensity-dependent photoresponse characteristics of the photodetector. Figure 3c plots the $I–V$ curves under 520 nm irradiation with varied light intensities. Remarkably, the photocurrent at both zero and reverse biases rose gradually with increase in light intensity (also see in Figure S4c, Supporting Information), which was attributed to the increased amount of photocarriers at an elevated light intensity. Also, it was observed that the photocurrent at zero bias first increased rapidly from ≈15.5 pA to ≈0.26 nA when light intensity was changed from 9 to 316 μW cm^{-2}, and further increase of light intensity from 316 μW cm^{-2} to 27.12 mW cm^{-2} led to a slow increase of photocurrent only from ≈0.26 to ≈0.74 nA. To gain insight into the dependence of photocurrent on light intensity, the curve of photocurrent at zero bias versus light intensity was then fitted by a widely used power law: $I_{ph} \propto P^\theta$, where I_{ph} and P denote photocurrent
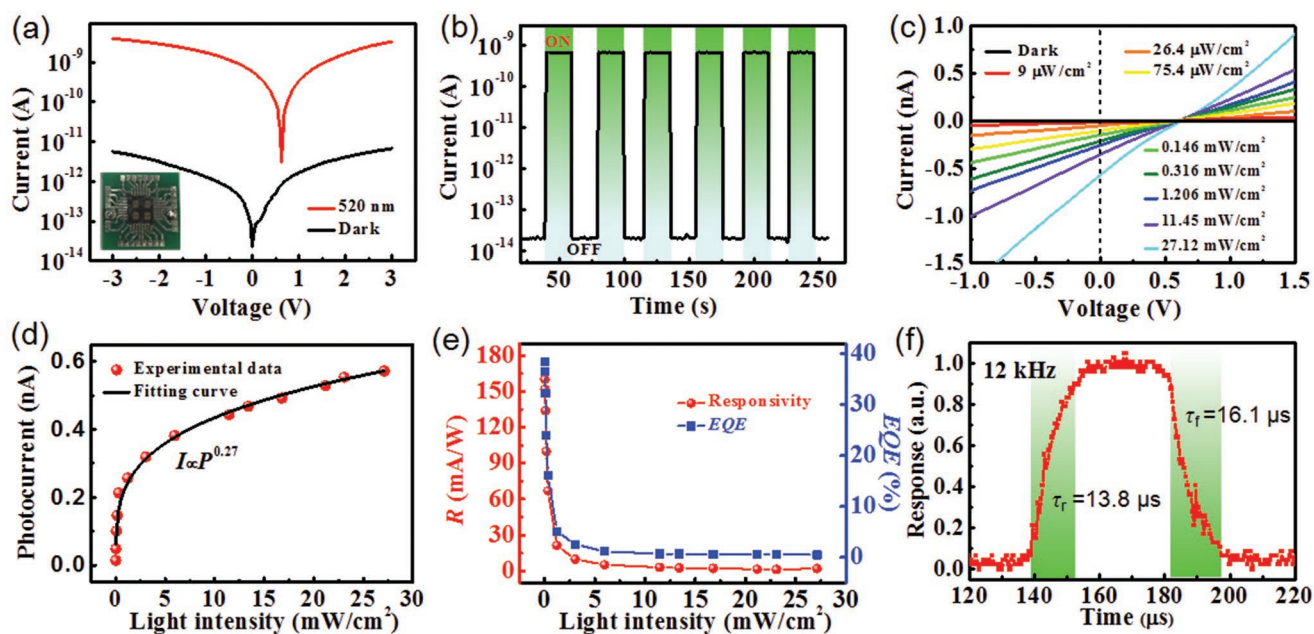

Figure 3. Electrical characterization of $CH_3NH_3PbI_3$ MWs array based photodetector with Au/Ag electrode pair. a) $I–V$ curves in dark and upon 520 nm light illumination (27.12 mW cm^{-2}). Inset shows a digital photograph of as-prepared devices fixed onto a printed circuit board. b) Time-dependent photoresponse at zero bias. c) $I–V$ curves upon 520 nm light illumination with varied light intensities. d) Photocurrent as a function of the incident light intensity. e) Responsivity and EQE as a function of the incident light intensity at zero bias. f) Photoresponse under a pulsed incident light with a frequency of 12 kHz.

ADVANCED
SCIENCE NEWS
www.advancedsciencenews.com

ADVANCED
ELECTRONIC
MATERIALS
www.advelectronicmat.de

($I_{ph} = I_{light} - I_{dark}$) and light intensity, respectively, and the exponent θ reflects the recombination activity of photocarriers.[45] As shown in Figure 3d, a low θ value of only 0.27 was obtained, which deviates largely from the ideal value of 1, and suggests the presence of strong recombination loss in the current device.[46] Therefore, it is expected that the device performance could be further improved by optimizing the device geometry such as shrinking the device channel, doping the $CH_3NH_3PbI_3$ MWs and so on.

To assess the performance of the present device in a more quantitative way, some key performance parameters including responsivity (R), external quantum efficiency (EQE), and specific detectivity ($D*$) were calculated. The R is defined as the generated photocurrent per unit power of light illumination per effective area, while the EQE is defined as the ratio between the number of photoexcited electron–hole pairs with contribution to photocurrent and the number of incident photons. The two parameters are usually given by the following equations[44]

$$R = \frac{I_{ph}}{PA} \tag{1}$$

$$EQE = R\frac{hc}{e\lambda} \tag{2}$$

where A is the effective illumination area (1×10^{-5} cm², the detailed estimation method is provided in the Supporting information); h, e, c, and λ represent Planck's constant, the elementary charge (1.6×10^{-19} C), the velocity of light and wavelength of incident light, respectively. According to the above equations, R and EQE were estimated to be 161.1 mA W^{-1} and 38.46%, respectively, at a low light intensity (9 μW cm^{-2}) at zero bias. Such a relatively large R value is comparable to or even better than a number of photodetectors involving $CH_3NH_3PbI_3$ perovskites with different morphologies or perovskite detectors operating on similar working mechanism (see **Table 1**).[25,26,36,47–49] Also, it was observed that both R and EQE values decreased gradually with increase in light intensity, as depicted in Figure 3e. Such a dependence of R and EQE with light intensity further manifests the existence of non-negligible recombination loss in the self-driven photodetector.

In addition, the $D*$ represents the capability of a photodetector to probe the weakest optical signal, and can be expressed as[50]

$$D* = \frac{(A\Delta f)^{1/2}}{NEP} \tag{3}$$

where Δf is the bandwidth and noise equivalent power (NEP) denotes the minimum incident optical power required to achieve a signal-to-noise ratio of unity at 1 Hz. The NEP is defined as[5]

$$NEP = \frac{\overline{i_n^2}^{1/2}}{R} \tag{4}$$

where $\overline{i_n^2}^{1/2}$ (in AHz$^{-1/2}$) is the root-mean-square value of the noise current in darkness. The $\overline{i_n^2}^{1/2}$ at 1 Hz was extracted to be as low as 3.6×10^{-16} AHz$^{-1/2}$ for our device by doing Fourier transformation of the dark current (Figure S5, Supporting Information). Consequently, the NEP was calculated to be 2.25×10^{-15} WHz$^{-1/2}$, which yields a large $D*$ of 1.3×10^{12} Jones.

Furthermore, we studied the response speed, which determines the capability of a detector to follow rapidly-switching light signal. As observed from a single cycle of photoresponse curve shown in Figure 3f, the device can operate properly with well distinguished on- and off-states under 520 nm irradiation with a modulation frequency of 12 kHz, indicating a rapid response speed. Accordingly, the rise and decay times were estimated to be 13.8/16.1 μs, respectively, determined by the duration required for the photoresponse to rise/decay from 10%/90% to 90%/10% of its peak value.[51] Significantly, the response speed of our self-driven photodetector is much faster than $CH_3NH_3PbI_3$ MWs/NWs-based photodetectors with symmetric contact electrodes and perovskite single-crystal photodetectors with asymmetric contact electrodes in previous reports (see Table 1).[25–27,48,49]

To shed light on the dependence of photoresponse on the incident light intensity, we then recorded normalized spectral response of the device in the wavelength region of 380–900 nm at a fixed light intensity. As plotted in **Figure 4**a, the detector exhibited a broadband photoresponse in the visible light regime, and the photoresponse declined steeply at ≈800 nm,

Table 1. Key performance figure-of-merits of photodetector in our work and other perovskite photodetectors in literatures.

Device structure	R [A W^{-1}]	$D*$ [Jones]	I_{light}/I_{dark} ratio	τ_r/τ_f	Operational bias [V]	Ref.
Au/$CH_3NH_3PbI_3$ MWs/Ag	0.16	1.3×10^{12}	3.3×10^4	13.8/16.1 μs	0	Our work
Au/$CH_3NH_3PbI_3$ NWs/Au	0.85	2.5×10^{12}	23	0.2/0.3 ms	1	[26]
Au/$CH_3NH_3PbI_3$ MWs/Au	13.57	5.25×10^{12}	–	80/240 μs	−5	[27]
Pt/$CH_3NH_3PbI_3$ NWs/Pt	0.005	–	–	0.25/0.35 ms	1	[25]
Au/$CH_3NH_3PbI_3$ network/Au	0.1	1.02×10^{12}	300	0.3/0.4 ms	10	[47]
ITO/$CH_3NH_3PbI_3$ film/ITO	0.0367	–	–	0.1/0.1 s	3	[36]
Au/$CH_3NH_3PbI_3$ single-crystal/Au	7.92	–	130	0.2/0.2 s	4	[52]
Au/$CH_3NH_3PbI_3$ single-crystal/Al	0.24	–	20	71/112 μs	1	[48]
Pt/$CH_3NH_3PbBr_3$ single-crystal/Au	0.002	1.4×10^{10}	–	70/150 μs	0	[49]
Au/$CH_3NH_3PbI_3$ film/Au	0.418	1.22×10^{13}	–	80/80 ms	1	[35]

**ADVANCED
SCIENCE NEWS**
www.advancedsciencenews.com

**ADVANCED
ELECTRONIC
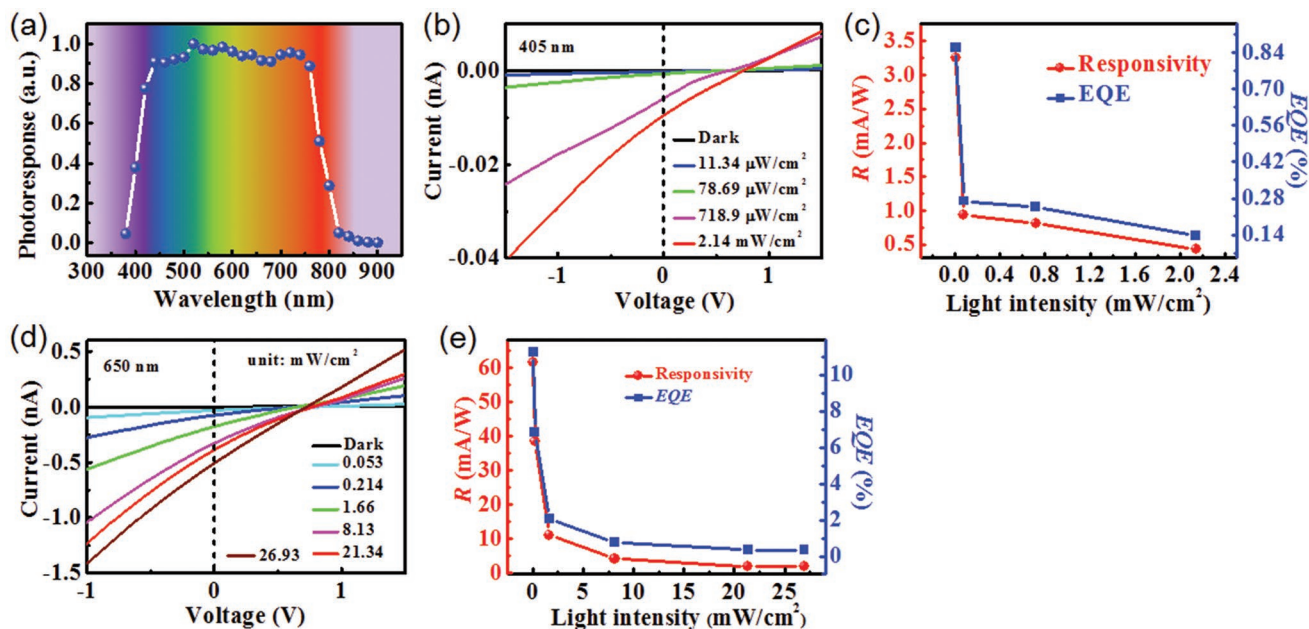MATERIALS**
www.advelectronicmat.de

Figure 4. a) Wavelength-dependent photoresponse of the device over the range from 380 to 900 nm. b) I–V curves and c) responsivity and EQE of the device under 405 nm light with varied light intensities at zero bias. d) I–V curves and (e) responsivity and EQE of the device under 650 nm light with varied light intensities at zero bias.

which was well consistent with the absorption spectrum of the $CH_3NH_3PbI_3$ MWs array (Figure 1d). To deeply understand wavelength-dependent photoresponse, the optoelectronic properties under 405 and 650 nm light illuminations with varying intensities were also studied. As shown in Figure 4b,d, the device showed apparent PV activities for both wavelengths. What is more, similar to what was observed under 520 nm irradiation, the photocurrents increased gradually with increasing light intensity as well (Figure S6, Supporting Information). In addition, we observed that the photocurrent upon 405 nm illumination was at least one order of magnitude lower that those under 520 and 650 nm illuminations at similar light intensity, which again manifests that the present detector had maximum photoresponse at visible light region. Further analysis of the R and EQE found that both values declined monotonously with increase in light intensity similarly, as displayed in Figure 4c,e. The R and EQE were estimated to be 3.26 mA W^{-1} and 0.86%, respectively, for 405 nm irradiation (11.34 μW cm^{-2}), which increased to as high as 61.5 mA W^{-1} and 11.26%, respectively, for 650 nm irradiation (53 μW cm^{-2}).

Figure 5 and Table 1 summarized the key performance figure-of-merits of the self-driven photodetector in this work and some representative perovskite photodetectors reported in literatures. Significantly, our device with Au/Ag asymmetric electrodes exhibited not only comparable or even higher responsivity and specific detectivity, but also much faster response speed than those of detectors made from $CH_3NH_3PbI_3$ perovskites with various morphologies, or perovskite photodetectors working on similar operational principle.

Flexible photodetectors are of particular importance for a range of emerging applications such as stretchable and wearable optoelectronics, implantable biomedical devices and so on.[23,24] The facile solution-based preparation method enables

our self-driven photodetectors to be assembled on plastic substrates. **Figure 6**a,b displays the schematic diagram and an optical photography of typical $CH_3NH_3PbI_3$ MWs array-based photodetectors with Au/Ag electrode pair on a polyvinyl chloride (PVC) substrate, respectively. The flexible photodetector was characterized by recording the time-dependent photoresponse under 520 nm light illumination (27.12 mW cm^{-2}) before and after bending for various times, as well as being bent to varied radii. As shown in Figure 6c, the flexible photodetector showed comparable photoresponse characteristics with those of devices on rigid substrates before bending. The
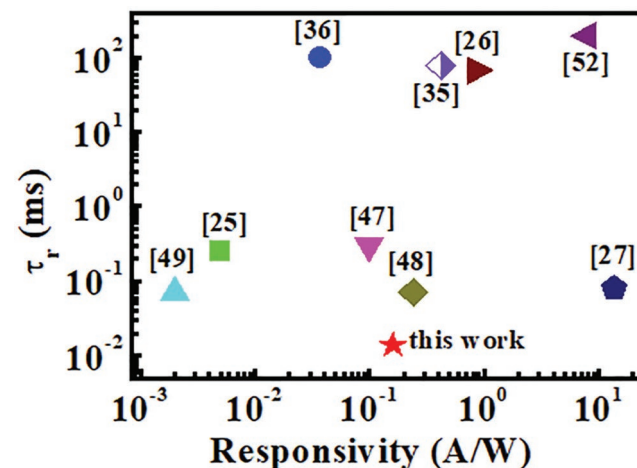

Figure 5. Comparison of responsivity and rise time of the self-driven photodetector in this work with other perovskite photodetectors reported in literatures.
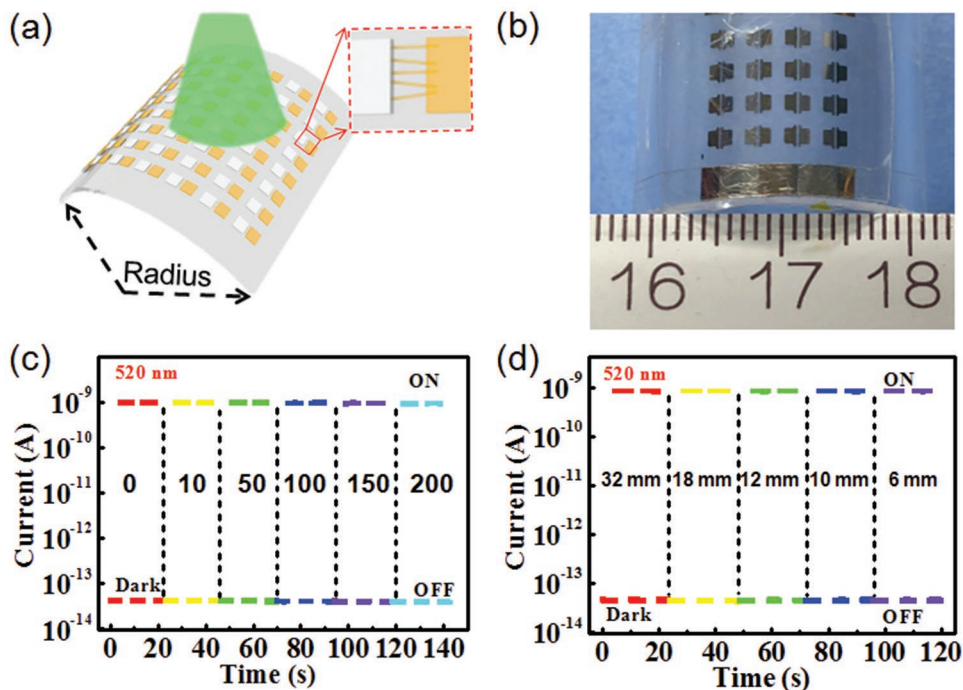
Figure 6. a) Schematic illustration of the flexible $CH_3NH_3PbI_3$ MWs array based photodetector. b) Photograph of as-fabricated devices under bending condition. c) Dark current and photocurrent of the flexible photodetector without bending and after 5, 10, 100, 150, and 200 cycles of bending with a bending radius of 18 mm. d) Dark current and photocurrent of the flexible photodetector being bent to various radii.

slightly larger photocurrent and dark current may be ascribed to higher density of MWs within the device channel. Importantly, the device can retain the good photoresponse properties even after bending for hundreds of repetitions with a nearly negligible decline in both photocurrent and dark current, which was likely caused by cracks emerged in the metal electrodes after many times of bending. In addition, as observed in Figure 6d, the photocurrent and dark current are almost invariant of the bending radius, and the detector can operate properly even being bent to a radius as low as 6 mm. The totality of the above results suggests that the $CH_3NH_3PbI_3$ MW arrays-based self-driven photodetectors on flexible substrate hold excellent flexibility and bending durability.

3. Conclusion

To conclude, self-driven perovskite photodetectors have been developed by designing asymmetric contact electrodes on opposite ends of $CH_3NH_3PbI_3$ MWs array, which was synthesized by a simple one-step self-assembly method. Benefiting from the strong built-in potential induced by asymmetric electrodes with varied work functions, the as-fabricated devices showed apparent PV activities, providing our devices with the opportunity to operate without exterior power supply. It was observed that the $CH_3NH_3PbI_3$ MWs array-based devices were highly sensitive to visible light illumination. Upon 520 nm irradiation, a typical photodetector with Au/Ag electrode pair attained a respectable responsivity of 161.1 mA W^{-1}, and a high specific detectivity of 1.3×10^{12} Jones thanks to the ultralow dark current. What is more, a fast response speed

with rise/decay time of 13.8/16.1 µs was also achieved. In addition, flexible photodetectors assembled on polymer substrates possessed comparable photoresponse performance, and outstanding mechanical flexibility and bending durability. The overall good performance together with the simple device geometry suggests that the present self-driven photodetectors may find potential application in future low energy consumption optoelectronic systems.

4. Experimental Section

Material Preparation and Characterization: $CH_3NH_3PbI_3$ MWs were prepared through a one-step solvent evaporation induced self-assembly method according to a previous report.[26] In a typical procedure, 46.1 mg PbI$_2$ (Aldrich, 99%) and 15.9 mg MAI (Aldrich, 99.5%) were sequentially dissolved in 6.4 mL *N,N*-dimethylformamide (DMF, 99.8%) to obtain a $CH_3NH_3PbI_3$ precursor solution. The as-mixed solution was stirred at 60 °C for 2 h to get a clear and transparent solution before use. A precleaned Si/SiO$_2$ substrate was treated by oxygen plasma for 10 min to obtain a hydrophilic surface. Then the substrate was leaned on a slide glass with a tilting angle of about 10°, and 3 µL as-prepared $CH_3NH_3PbI_3$ precursor solution was dripped onto the substrate, which spread naturally and distributed on the substrate uniformly. After naturally dried at room temperature for about 2 h, $CH_3NH_3PbI_3$ MWs with aligned growth direction were obtained on the substrate. Finally, the substrate was thermally annealed at 75 °C for 10 min to improve the crystallinity of the MWs. The morphologies and microstructures of the $CH_3NH_3PbI_3$ MWs were characterized by field emission scanning electron microscopy (Hitachi SU8020) and X-ray diffraction (Rigaku D/max-γ B, with Cu Kα radiation). The absorption spectrum was recorded on a Shimadzu UV-2550 UV–vis spectrophotometer. The PL spectrum of $CH_3NH_3PbI_3$ MWs was measured by HR Evolution (Horiba Jobin Yvon) Raman spectrometer with a 532 nm laser.

**ADVANCED
SCIENCE NEWS**
www.advancedsciencenews.com

**ADVANCED
ELECTRONIC
MATERIALS**
www.advelectronicmat.de

Device Fabrication and Analysis: To fabricate photodetectors with symmetric contact electrodes, 50 nm Au or Ag was deposited onto opposite ends of the MWs grown on SiO_2/Si substrate by electron beam evaporation through a lab-built shadow mask with a channel length of 100 µm. In order to construct photodetectors with asymmetric contact electrodes, a high work function metal electrode (50 nm Au or Pt) was first deposited on one end of the MWs by sheltering the hollow pattern of the shadow mask atop another end of the MWs. Then, a low work function metal electrode (50 nm Ag, Au, or Ti) was deposited on another end of the MWs by repeating the above process. Flexible photodetectors were fabricated in a similar way on flexible plastic substrate. The electrical characterization of the devices was performed by using a semiconductor characterization system (4200-SCS, Keithley Co. Ltd.) equipped with a monochromator (SP 2150, Princeton Co.). Laser diodes with different wavelengths (405 nm (LP405-SF10), 520 nm (LP520-SF15), and 650 nm (L650P007)) were used as light sources. The power intensity of all light sources was carefully calibrated using a power meter (Thorlabs GmbH., PM 100D) before measurement. For response speed study, a signal generator (Tektronix, TDS2022B) was employed to power the laser diode to produce pulsed light of varied frequencies, and an oscilloscope (Tektronix, TDS2012B) was used to record the output electrical data. All measurements were performed in ambient conditions at room temperature.

Supporting Information

Supporting Information is available from the Wiley Online Library or from the author.

Acknowledgements

Conflict of Interest

The authors declare no conflict of interest.

Keywords

[1] Y. Zhao, K. Zhu, *Chem. Soc. Rev.* **2016**, *45*, 655.
[2] Q. Chen, N. De Marco, Y. Yang, T. Bin Song, C. C. Chen, H. Zhao, Z. Hong, H. Zhou, Y. Yang, *Nano Today* **2015**, *10*, 355.
[3] H. Zhou, Q. Chen, G. Li, S. Luo, T.-b. Song, H.-S. Duan, Z. Hong, J. You, Y. Liu, Y. Yang, *Science* **2014**, *345*, 542.
[4] Y. Ling, Z. Yuan, Y. Tian, X. Wang, J. C. Wang, Y. Xin, K. Hanson, B. Ma, H. Gao, *Adv. Mater.* **2016**, *28*, 305.
[5] C. Xie, P. You, Z. Liu, L. Li, F. Yan, *Light: Sci. Appl.* **2017**, *6*, e17023.
[6] H. Zhu, Y. Fu, F. Meng, X. Wu, Z. Gong, Q. Ding, M. V. Gustafsson, M. T. Trinh, S. Jin, X.-Y. Zhu, *Nat. Mater.* **2015**, *14*, 636.
[7] C.-H. Lin, B. Cheng, T.-Y. Li, J. R. D. Retamal, T.-C. Wei, H.-C. Fu, X. Fang, J.-H. He, *ACS Nano* **2018**, *13*, 1168.
[8] C. Xie, F. Yan, *J. Mater. Chem. C* **2018**, *6*, 1338.
[9] B. Saparov, D. B. Mitzi, *Chem. Rev.* **2016**, *116*, 4558.
[10] J. Y. Han, J. Wang, M. Yang, X. Kong, Z. H. Huang, H. Guo, S. L. Tao, Z. J. Liu, Z. M. Wu, Y. D. Jiang, X. R. Wang, *Adv. Mater.* **2018**, *30*, 1804020.
[11] A. M. Al-Amri, B. Cheng, J.-H. He, *IEEE Trans. Nanotechnol.* **2019**, *18*, 1.
[12] H. Wang, D. H. Kim, *Chem. Soc. Rev.* **2017**, *46*, 5204.
[13] M. Ahmadi, T. Wu, B. Hu, *Adv. Mater.* **2017**, *29*, 1605242.
[14] J. Zhou, J. Huang, *Adv. Sci.* **2018**, *5*, 1700256.
[15] W. Tian, H. Zhou, L. Li, *Small* **2017**, *13*, 1702107.
[16] B. Cheng, T. Y. Li, P. C. Wei, J. Yin, K. T. Ho, J. R. D. Retamal, O. F. Mohammed, J. H. He, *Nat. Commun.* **2018**, *9*, 5196.
[17] Z. Chu, M. Yang, P. Schulz, D. Wu, X. Ma, E. Seifert, L. Sun, X. Li, K. Zhu, K. Lai, *Nat. Commun.* **2017**, *8*, 2230.
[18] J.-W. Lee, S.-H. Bae, N. De Marco, Y.-T. Hsieh, Z. Dai, Y. Yang, *Mater. Today Energy* **2018**, *7*, 149.
[19] X. Li, M. Ibrahim Dar, C. Yi, J. Luo, M. Tschumi, S. M. Zakeeruddin, M. K. Nazeeruddin, H. Han, M. Grätzel, *Nat. Chem.* **2015**, *7*, 703.
[20] D. Shi, V. Adinolfi, R. Comin, M. Yuan, E. Alarousu, A. Buin, Y. Chen, S. Hoogland, A. Rothenberger, K. Katsiev, Y. Losovyj, X. Zhang, P. A. Dowben, O. F. Mohammed, E. H. Sargent, O. M. Bakr, *Science* **2015**, *347*, 519.
[21] Q. Dong, Y. Fang, Y. Shao, P. Mulligan, J. Qiu, L. Cao, J. Huang, *Science* **2015**, *347*, 967.
[22] M. I. Saidaminov, A. L. Abdelhady, B. Murali, E. Alarousu, V. M. Burlakov, W. Peng, I. Dursun, L. Wang, Y. He, G. Maculan, A. Goriely, T. Wu, O. F. Mohammed, O. M. Bakr, *Nat. Commun.* **2015**, *6*, 7586.
[23] C. Xie, F. Yan, *Small* **2017**, *13*, 1701822.
[24] Z. Lou, G. Shen, *Adv. Sci.* **2016**, *3*, 1500287.
[25] E. Horváth, M. Spina, Z. Szekrényes, K. Kamarás, R. Gaal, D. Gachet, L. Forró, *Nano Lett.* **2014**, *14*, 6761.
[26] H. Deng, D. Dong, K. Qiao, L. Bu, B. Li, D. Yang, H.-E. Wang, Y. Cheng, Z. Zhao, J. Tang, H. Song, *Nanoscale* **2015**, *7*, 4163.
[27] W. Deng, X. Zhang, L. Huang, X. Xu, L. Wang, J. Wang, Q. Shang, S. T. Lee, J. Jie, *Adv. Mater.* **2016**, *28*, 2201.
[28] Q. Hu, H. Wu, J. Sun, D. Yan, Y. Gao, J. Yang, *Nanoscale* **2016**, *8*, 5350.
[29] W. Deng, L. Huang, X. Xu, X. Zhang, X. Jin, S.-T. Lee, J. Jie, *Nano Lett.* **2017**, *17*, 2482.
[30] C. Xie, Y. Wang, Z. X. Zhang, D. Wang, L. B. Luo, *Nano Today* **2018**, *19*, 41.
[31] Z.-X. Zhang, L-H. Zeng, X.-W. Tong, Y. Gao, C. Xie, Y. H. Tsang, L.-B. Luo, Y.-C. Wu, *J. Phys. Chem. Lett.* **2018**, *9*, 1185.
[32] H. Sun, W. Tian, F. Cao, J. Xiong, L. Li, *Adv. Mater.* **2018**, *30*, 1706986.
[33] F. Cao, L. Meng, M. Wang, W. Tian, L. Li, *Adv. Mater.* **2019**, *31*, 1806725.
[34] Y. Zhang, W. Xu, X. Xu, J. Cai, W. Yang, X. Fang, *J. Phys. Chem. Lett.* **2019**, *10*, 836.
[35] S.-F. Leung, K.-T. Ho, P.-K. Kung, V. K. S. Hsiao, H. N. Alshareef, Z. L. Wang, J.-H. He, *Adv. Mater.* **2018**, *30*, 1704611.
[36] X. Hu, X. Zhang, L. Liang, J. Bao, S. Li, W. Yang, Y. Xie, *Adv. Funct. Mater.* **2014**, *24*, 7373.
[37] S. M. Sze, K. K. Ng, *Physics of Semiconductor Devices*, Wiley, New York **2007**.
[38] W. J. Yu, Y. Liu, H. Zhou, A. Yin, Z. Li, Y. Huang, X. Duan, *Nat. Nanotechnol.* **2013**, *8*, 952.
[39] L. Britnell, R. M. Ribeiro, A. Eckmann, R. Jalil, B. D. Belle, A. Mishchenko, Y.-J. Kim, R. V Gorbachev, T. Georgiou,

S. V Morozov, A. N. Grigorenko, A. K. Geim, C. Casiraghi, A. H. C. Neto, K. S. Novoselov, *Science* **2013**, *340*, 1311.

[40] Y. Liu, R. Cheng, L. Liao, H. Zhou, J. Bai, G. Liu, L. Liu, Y. Huang, X. Duan, *Nat. Commun.* **2011**, *2*, 579.

[41] W. Yu, F. Li, L. Yu, M. R. Niazi, Y. Zou, D. Corzo, A. Basu, C. Ma, S. Dey, M. L. Tietze, U. Buttner, X. Wang, Z. Wang, M. N. Hedhili, C. Guo, T. Wu, A. Amassian, *Nat. Commun.* **2018**, *9*, 5354.

[42] L. H. Zeng, M. Z. Wang, H. Hu, B. Nie, Y. Q. Yu, C. Y. Wu, L. Wang, J. G. Hu, F. X. Liang, L. B. Luo, *ACS Appl. Mater. Interfaces* **2013**, *5*, 9362.

[43] Y. Ning, Z. Zhang, F. Teng, X. Fang, *Small* **2018**, *14*, 1703754.

[44] C. Xie, C. Mak, X. Tao, F. Yan, *Adv. Funct. Mater.* **2017**, *27*, 1603886.

[45] L. H. Zeng, S. H. Lin, Z. J. Li, Z. X. Zhang, T. F. Zhang, C. Xie, C. H. Mak, Y. Chai, S. P. Lau, L. B. Luo, Y. H. Tsang, *Adv. Funct. Mater.* **2018**, *28*, 1705970.

[46] X. Li, M. Zhu, M. Du, Z. Lv, L. Zhang, Y. Li, Y. Yang, T. Yang, X. Li, K. Wang, H. Zhu, Y. Fang, *Small* **2016**, *12*, 595.

[47] H. Deng, X. Yang, D. Dong, B. Li, D. Yang, S. Yuan, K. Qiao, Y.-B. Cheng, J. Tang, H. Song, *Nano Lett.* **2015**, *15*, 7963.

[48] J. Ding, H. Fang, Z. Lian, J. Li, Q. Lv, L. Wang, J.-L. Sun, Q. Yan, *Cryst Eng Comm* **2016**, *18*, 4405.

[49] P. A. Shaikh, D. Shi, J. R. D. Retamal, A. D. Sheikh, M. A. Haque, C.-F. Kang, J.-H. He, O. M. Bakr, T. Wu, *J. Mater. Chem. C* **2016**, *4*, 8304.

[50] D. Wu, Y. Wang, L. Zeng, C. Jia, E. Wu, T. Xu, Z. Shi, Y. Tian, X. Li, Y. H. Tsang, *ACS Photonics* **2018**, *5*, 3820.

[51] R. Zhuo, Y. Wang, D. Wu, Z. Lou, Z. Shi, T. Xu, Y. Tian, X. Li, *J. Mater. Chem. C* **2018**, *6*, 299.

[52] H. Fang, Q. Li, J. Ding, N. Li, H. Tian, L. Zhang, T.-L. Ren, J. Dai, L. Wang, Q. Yan, *J. Mater. Chem. C* **2016**, *4*, 630.